

Latitudinal variability in Jupiter's tropospheric disequilibrium species: GeH_4 , AsH_3 and PH_3

R. S. Giles^{a,*}, L. N. Fletcher^b, P. G. J. Irwin^a

^a*Atmospheric, Oceanic & Planetary Physics, Department of Physics, University of Oxford, Clarendon Laboratory, Parks Road, Oxford, OX1 3PU, UK*

^b*Department of Physics and Astronomy, University of Leicester, University Road, Leicester, LE1 7RH, UK*

Abstract

Jupiter's tropospheric composition is studied using high resolution spatially-resolved 5- μm observation from the CRIRES instrument at the Very Large Telescope. The high resolving power ($R=96,000$) allows us to spectrally resolve the line shapes of individual molecular species in Jupiter's troposphere and, by aligning the slit north-south along Jupiter's central meridian, we are able to search for any latitudinal variability. Despite the high spectral resolution, we find that there are significant degeneracies between the cloud structure and aerosol scattering properties that complicate the retrievals of tropospheric gaseous abundances and limit conclusions on any belt-zone variability. However, we do find evidence for variability between the equatorial regions of the planet and the polar regions. Arsine (AsH_3) and phosphine (PH_3) both show an enhancement at high latitudes, while the abundance of germane (GeH_4) remains approximately constant. These observations contrast with the theoretical predictions from Wang et al. (2016) and we discuss the possible explanations for this difference.

Keywords: Jupiter, Atmospheres, composition, Atmospheres, structure

1. Introduction

The 5- μm atmospheric window is a unique region of Jupiter's spectrum where a dearth of opacity from the planet's principal infrared absorbers gives us access to parts of the atmosphere that are otherwise hidden from view. In the absence of clouds, the sensitivity of the 4.5–5.2 μm spectrum peaks in the 4–8 bar region of Jupiter's atmosphere (Giles et al., 2015). These pressure levels correspond to Jupiter's middle troposphere, a region of the planet that is home to many interesting phenomena, including multiple cloud layers, disequilibrium chemical species and dynamics ranging from small-scale meteorological features to planetary-scale overturning.

The atmospheric window was first described by Gillett et al. (1969) and the high degree of spatial variability was noted by Westphal (1969). The brightness at 5- μm is very sensitive to the opacity of the tropospheric clouds; in the relatively cloud-free belts, the bright radiation from depth can be observed, but this is partially shielded by the thicker clouds in the zones. Since then, the 5- μm region has been the focus of many studies, from ground-based telescopes, airborne observatories and spacecraft. Ground-based and airborne telescopes generally offer a higher spectral resolution, so these observations are well suited to the study of individual gaseous species in the troposphere.

Bjoraker et al. (1986) used data from the Kuiper Airborne Observatory to determine the tropospheric composition, and a similar analysis was carried out by Encrenaz et al. (1996) using the Infrared Space Observatory. The United Kingdom Infrared Telescope, Canada-France-Hawaii Telescope and the Keck Observatory have been used by several groups in order to target individual gaseous species in discrete regions of the planet (Bézard et al., 2002; Noll et al., 1989; Bjoraker et al., 2015).

Germane (GeH_4), arsine (AsH_3) and phosphine (PH_3) are all disequilibrium species in Jupiter's troposphere. Their abundances are determined by temperature-dependent equilibrium reactions and deep in the atmosphere, the temperature is high enough that they are chemically stable. The temperature in the observable troposphere is much lower so we would expect the abundances to rapidly drop off (e.g. Fegley and Lodders, 1994). However, GeH_4 , AsH_3 and PH_3 have all been detected in Jupiter's 5- μm window with higher abundances than would be expected from equilibrium chemistry (Fink et al., 1978; Noll et al., 1989; Ridgway et al., 1976). Further background about GeH_4 , AsH_3 and PH_3 are given in Sections 6, 7 and 8 respectively.

The apparently enhanced abundances are indicative of rapid vertical mixing, which brings the disequilibrium species upwards from deeper pressures where they are more abundant. Instead of dropping off rapidly with altitude, the abundance is “frozen in” at a roughly constant value. This observed abundance corresponds to the equi-

*Corresponding author

Email address: rohini.giles@physics.ox.ac.uk (R. S. Giles)

librium abundance at a much deeper level, known as the “quench level”, which depends on both the strength of vertical mixing and the chemical kinetic rates (Lewis and Fegley, 1984). In the case of PH_3 , the quench level is ~ 900 K, which corresponds to >100 bar (Wang et al., 2016). This means that disequilibrium species such as GeH_4 , AsH_3 and PH_3 act as tracers of atmospheric dynamics in Jupiter’s troposphere (Taylor et al., 2004).

Because vertical mixing strengths vary as a function of latitude (Flasar and Gierasch, 1978; Wang et al., 2015), the tropospheric abundances of these species are also expected to vary. Wang et al. (2016) recently carried out a theoretical study where they combined diffusion-kinetics calculations with estimates for how Jupiter’s eddy diffusion coefficient varies with latitude, in order to predict the latitudinal distribution of disequilibrium species, including GeH_4 , AsH_3 and PH_3 . Because of the different kinetics rates for the different gases, they predict that the GeH_4 abundance should be a maximum in the equatorial latitudes, and decrease towards the poles, while AsH_3 and PH_3 should be latitudinally uniform.

In this paper, we use high-resolution ground-based observations from the CRIRES instrument at the Very Large Telescope in Chile to search for evidence of latitudinal variability in Jupiter’s tropospheric composition. In Sections 2 and 3 we describe our observations and our atmospheric retrieval algorithm. In Sections 4 and 5 we discuss the effect of cloud structure and scattering properties on the atmospheric retrievals. In Sections 6, 7 and 8 we measure the abundances of GeH_4 , AsH_3 and PH_3 respectively. The results of these sections are then discussed in Section 9.

2. Observations

2.1. CRIRES observations

Observations of Jupiter 5- μm window were made using CRIRES, a cryogenic high-resolution infrared echelle spectrograph (Käufl et al., 2004), located at the European Southern Observatory’s Very Large Telescope (VLT). The instrument provides long-slit ($0.2 \times 40''$) spectroscopy across the wavelength range $0.95\text{--}5.38\ \mu\text{m}$, with a resolving power of 96,000.

The observations were made on 12 November 2012 (05:00–05:40 UT) and 1 January 2013 (02:50–03:30 UT). The atmospheric conditions were better on 12 November 2012, so the majority of this work focuses on those observations. However, the observations from 1 January 2013 are used in Sections 7 and 8 to show that the same conclusions can be drawn from both datasets.

On both dates, the slit was aligned north-south on Jupiter, along the planet’s central meridian, allowing us to measure spatial variability with latitude, but not longitude. Figure 1 shows the acquisition image of Jupiter made on 12 November, using a Ks-band filter ($2.2\ \mu\text{m}$). The vertical black line shows how the narrow slit was aligned. The slit length ($40''$) was smaller than the angular diameter of

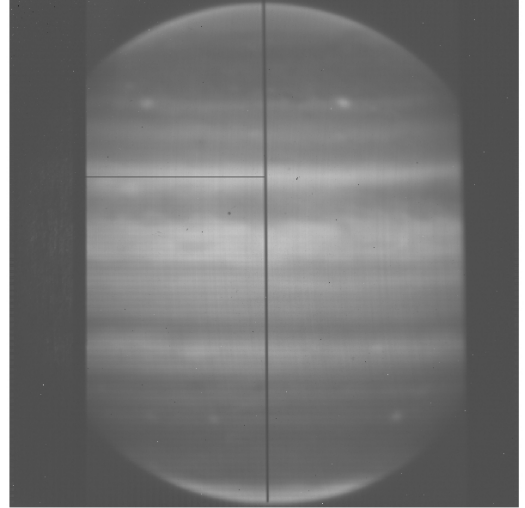


Figure 1: Acquisition image of Jupiter made at 05:02 UT on 12 November 2012, immediately before the 5- μm observations. This image was made using a Ks-band filter ($2.2\ \mu\text{m}$). The vertical black line shows the alignment of the narrow slit.

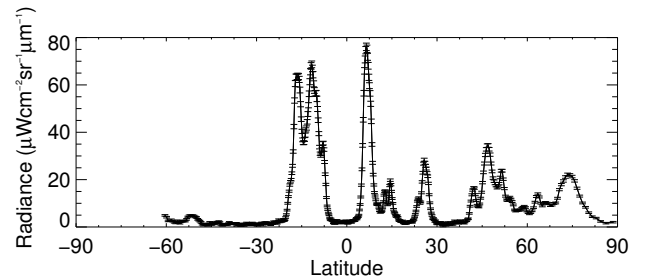


Figure 2: Measured radiance at $5.0\ \mu\text{m}$ as a function of latitude.

Jupiter on the observation dates ($47\text{--}48''$), so the observations cut off the southern polar region. Figure 2 shows the observed radiance as a function of latitude at $5.0\ \mu\text{m}$. The high degree of spatial variability between the belts and the zones is due to the varying opacity of the tropospheric clouds.

On each date, observations were made in 14 different wavelength settings, which together cover the entire $4.55\text{--}5.26\ \mu\text{m}$ wavelength range. The time lag between the first and last observation was ~ 40 minutes; during this time period, Jupiter rotated $\sim 25^\circ$, so the 14 different observations of different spectral regions do not correspond to precisely the same locations on the planet.

Observations were made of a standard star in order to provide radiometric calibration. Pi-2 Orionis (HIP 22509) and Zeta Tauri (HIP 26451) were used for the November and January observations respectively. Dark images and flatfields were also taken.

2.2. Data reduction

Initial data reduction was performed using EsoRex, the ESO Recipe Execution Tool (Ballester et al., 2006). The flatfields, darks, and nodded pairs of observations were used to produce a single combined observation of Jupiter for each of the 14 wavelength segments. The same process was applied to the observations of the standard star. In both cases, wavelength calibration was achieved by comparing telluric absorption lines with the HITRAN line database (Rothman et al., 2009). EsoRex was also used to calculate the background noise on both the stellar and the planetary observations.

Subsequent data reduction was performed independently of the EsoRex software. This included straightening the observations, to correct observed shears in both the spectral and spatial directions. The spectral shear was corrected using the wavelength calibration map generated by EsoRex. The spatial shear was cross-correlating by cross-correlating the north-south latitudinal profiles at different wavelengths i.e. requiring the belts and zones to be located at the same pixel values for all wavelengths. The jovian spectra were divided through by the standard star observations in order to remove the telluric lines, and were multiplied by the standard star reference spectrum to convert Jupiter’s photon count into spectral radiance. For Pi-2 Orionis, the standard star reference spectrum was provided by EsoRex. For Zeta Tauri, a black-body curve was scaled to match the observed magnitudes from the 2MASS all-sky survey (Cutri et al., 2003). Because the slit is very narrow, some stellar flux will be lost; this was accounted for in the radiometric calibration by assuming that the star is centrally placed in the slit, using a measurement of the star’s point spread function made in the perpendicular direction. Once this calibration has been applied, we find that the 5- μ m brightness temperatures vary between ~ 190 K in the coolest parts of the planet and ~ 260 K in the brightest regions (see Figure 2), which is roughly consistent with the 180-240 K range found in the Cassini VIMS 5- μ m observations (Giles et al., 2015). The noise on the spectra is roughly 5-10%, but this does not include the systematic error that could be introduced by the assumptions in the radiometric calibration. These systematic errors could increase or decrease the average radiance, but will not alter the shape of the spectra. The average radiance is primarily determined by the opacity of the upper cloud deck (Giles et al., 2015). Uncertainties in the radiometric calibration can therefore alter the apparent thickness of the clouds, but will not affect the analysis of the molecular species.

Geometric data was calculated using information from JPL HORIZONS, and by assuming that the slit was aligned with the central meridian. Planetocentric latitudes were assigned to each pixel using information about Jupiter’s angular size at the observation time, the angular size of each pixel, the centre-of-target latitude, and the location of the planet’s limb. In addition, the emission an-

gle, solar zenith angle and azimuthal angle were calculated for each pixel.

Due to Jupiter’s rotation, each of the 14 wavelength segments observed a slightly different longitude, with a $\sim 25^\circ$ difference between the first and last segment. Because Jupiter is longitudinally inhomogeneous, this means that each wavelength segment is observing a different cloud opacity; this prevents the different segments from being joined together into a single continuous observation. These latitudinally resolved spectra will be used in the following sections in order to search for variability in the deep cloud structure (Section 5) and in the abundances of germane, arsine and phosphine (Sections 6-8).

3. Spectral modelling

The CRILES spectra were analysed with the NEMESIS retrieval algorithm developed by Irwin et al. (2008). NEMESIS uses a radiative transfer code to compute the top-of-atmosphere spectral radiance for a given atmospheric profile, and then iteratively adjusts the atmospheric parameters in order to produce an optimal fit to the observed spectrum. For this work, we use line-by-line calculations in the radiative transfer code; previous work has made use of the correlated-k approximation (e.g. Giles et al., 2015) but the high spectral resolution of the CRILES observations means that this approximation would not save significant computational time. We therefore use the more accurate line-by-line method. The majority of the spectral line data were obtained from the HITRAN 2008 (Rothman et al., 2009) or GEISA 2009 (Jacquinot-Husson et al., 2011) molecular databases. The two exceptions are AsH₃, where we use laboratory data from Dana et al. (1993) and Mandin et al. (1995), and GeH₄, where we use the Spherical Top Data System (Wenger and Champion, 1998, see Section 6.1 for more details). Collision-induced absorption data is taken from Borysow and Frommhold (1986), Borysow and Frommhold (1987), Borysow et al. (1988) and Borysow (1991). We add a conservative 5% forward modelling error to the retrieval calculations, to take into account inaccuracies in the model (e.g. line data).

NEMESIS has the ability to model a multiple scattering atmosphere using the plane-parallel matrix operator method of Plass et al. (1973), and we show in Section 4 that the scattering properties of Jupiter’s clouds have significant effects on the retrieved gaseous abundances. Unless otherwise stated, we use the simple cloud model from Giles et al. (2015): a single, spectrally-flat, compact cloud layer, located at 0.8 bar, with a single-scattering albedo $\omega = 0.9$ and a Henyey-Greenstein asymmetry parameter $g = 0.8$.

The reference atmospheric profile is described as in Giles et al. (2015). The gaseous species with spectral features in the 5- μ m region are NH₃, PH₃, CO, GeH₄, AsH₃, H₂O and CH₃D. Unless otherwise stated, the abundances of

each of these gases are allowed to vary via a single scaling parameter.

4. Scattering properties of upper cloud

The high spectral resolution of the CRIRES instrument allows us to resolve the individual absorption lines of molecular species in Jupiter’s troposphere. Using the NEMESIS retrieval algorithm, we can retrieve the abundances of gases, and map how these abundances vary across the planet. The high spectral resolution helps to reduce the degeneracy between different gaseous species. However, there is a degeneracy between the gaseous abundances and scattering parameters of Jupiter’s tropospheric clouds: specifically, the asymmetry parameter, g , which defines the extent to which the cloud particles are forward scattering.

An example of this effect is shown in Figure 3. This figure shows three prominent CH_3D absorption features, marked by the horizontal double-headed arrows. The CRIRES data are shown in black, and is from the Equatorial Zone of the planet. The Equatorial Zone was chosen as it is one of the cloudiest regions of the planet. Small segments of data with high error bars (due to telluric contamination) have been removed. The three absorption features were fitted simultaneously, and the coloured lines show the fits that can be obtained using two different assumptions about the scattering properties of the single cloud deck. Both cases can produce a good fit to the broad CH_3D features, but the retrieved CH_3D abundances are significantly different: 0.16 ppm for the case where $g = 0.4$ and 0.08 ppm for the case where $g = 0.9$.

This effect is due to the different amount of reflected sunlight in the two models. A higher asymmetry parameter (more forward scattering) leads to a higher fraction of radiation originating from the planet, and a lower fraction from reflected sunlight. In contrast, a lower asymmetry parameter (less forward scattering) leads to a higher fraction due to reflected sunlight. A higher g value therefore leads to stronger absorption features for a given gaseous abundance, and hence lower retrieved abundances. It should be noted that this is dependent on the vertical location of the cloud; if the cloud were located below the main line forming region, the effect would be less pronounced. However, Giles et al. (2015) showed that the main tropospheric cloud deck must be located well above the line forming in order to account for the highly variable 5- μm radiation.

This degeneracy between cloud scattering properties and retrieved gaseous abundances is only present in regions of the planet with thick cloud cover (zones like the Equatorial Zone). The belts of the planet are relatively cloud-free, so changing the cloud parameters has little impact on the retrievals. This means that different assumptions about the cloud properties can affect the latitudinal profiles of the gases; one set of parameters could suggest that a molecular species has a constant abundance across the planet, while another set of parameters could suggest

| g | χ^2/N |
|-------------|-------------|
| 0.40 | 2.25 |
| 0.45 | 2.11 |
| 0.50 | 1.95 |
| 0.55 | 1.80 |
| 0.60 | 1.66 |
| 0.65 | 1.54 |
| 0.70 | 1.43 |
| 0.75 | 1.31 |
| 0.80 | 1.19 |
| 0.85 | 1.52 |
| 0.90 | 2.40 |

Table 1: The goodness-of-fit values (χ^2/N) for a range of different asymmetry parameters. χ^2/N is minimised when $g = 0.8$.

that the abundance varies between belts and zones. Selecting the correct scattering parameters is therefore of critical importance.

In Giles et al. (2015) we constrained the scattering parameters of Jupiter’s tropospheric clouds using limb darkening observations from the VIMS instrument on the Cassini spacecraft. This analysis ruled out strongly forward scattering particles ($g > 0.9$), but a broad range of values were consistent with the data. In order to further constrain the asymmetry parameter properties of the clouds, we can make use of the Fraunhofer lines that are present in the CRIRES data because of the reflected sunlight. These narrow solar absorption lines can be seen in Figure 3 (marked by the vertical single-headed arrows). The strength of these features also depends on the scattering properties: lower g values lead to higher fractions of reflected sunlight and deeper absorption features. Bjoraker et al. (2015) also made use of a Fraunhofer line at 4.67 μm to determine the reflectance of the upper tropospheric clouds.

We ran retrievals using a range of different g values in order to determine which value gave the best fit to the CRIRES data from the EqZ. The entire 5- μm spectral range was used, excluding regions with high error bars due to telluric contamination. For each value of g , the goodness-of-fit was calculated and the results are given in Table 1. The best fit was obtained for $g = 0.8$, which is consistent with previous analyses (Giles et al., 2015; Irwin et al., 2008). In the following sections, we will use a cloud with an asymmetry parameter $g = 0.8$. We also make the assumption that the asymmetry parameter does not vary with latitude. In each case, we will investigate the extent to which the results are dependent on the assumed asymmetry parameter.

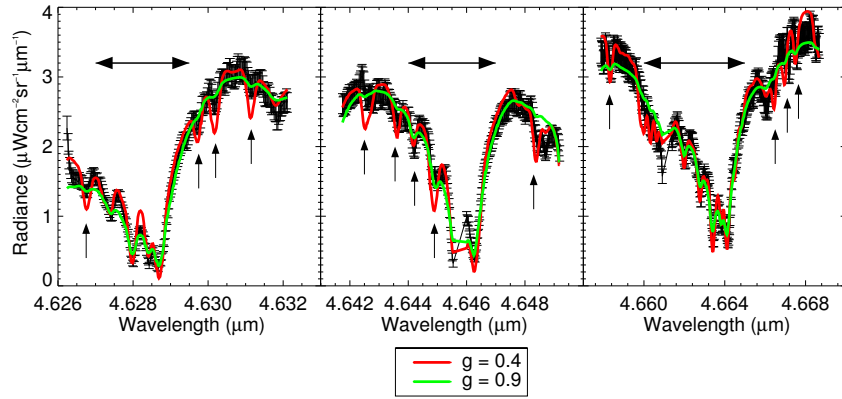


Figure 3: Fits to three CH_3D absorption features using two different values of the cloud particle asymmetry parameter, g . The observational data (black) is from the Equatorial Zone of Jupiter. The location of the CH_3D absorption features are marked by the horizontal double-headed arrows. The location of the most prominent Fraunhofer lines are marked by the vertical single-headed arrows.

5. CH_3D and the deep cloud structure

5.1. Introduction

Methane (CH_4) was one of the first gases to be discovered in Jupiter’s atmosphere when Wildt (1932) identified previously unknown spectral features as methane and ammonia absorption lines. It is the third most abundant gaseous species in Jupiter’s upper atmosphere, with a volume mixing ratio (VMR) of 2.04×10^{-3} in the troposphere detected by the Galileo Probe Mass Spectrometer (Wong et al., 2004). Unlike many other gaseous species, this abundance is not expected to have any spatial variability in the troposphere. This is because CH_4 is chemically stable throughout the troposphere and does not condense at the temperatures found in Jupiter’s atmosphere (Taylor et al., 2004), which means that it should be well-mixed.

As a methane isotopologue, CH_3D (deuterated methane) is also constant throughout Jupiter’s troposphere. Unlike CH_4 , no in situ measurements have been made of the jovian CH_3D abundance, but a tropospheric abundance of 0.16 ± 0.05 ppm has been estimated from observations made with the Infrared Space Observatory (Lellouch et al., 2001). The CH_3D abundance is particularly relevant to our study because CH_3D has several strong absorption features in the 5- μm window.

It is the spatial homogeneity of CH_3D that provides an opportunity to study Jupiter’s deep cloud structure. Because the CH_3D abundance is expected to be constant with latitude, any observed variation in the spectral lineshape must be due to another factor. One way of reproducing variable lineshapes is by varying the deep tropospheric cloud structure (Bjoraker et al., 2015). In this section, we will search for spatial variability in the CH_3D lineshapes, and will explore how this can be interpreted in terms of cloud structure.

5.2. Analysis

5.2.1. CH_3D

There are several CH_3D features in the 5- μm window. Three of the strongest features are shown in Figure 4. These three features are within the same wavelength segment, which means they are from the same longitude (i.e. were observed simultaneously) and can therefore be analysed simultaneously. The CRISP data are shown in black, and the arrows show the locations of the CH_3D features. The upper panel shows the data from the cool Equatorial Zone (EqZ, 5°S - 4°N), while the lower panel shows data from the warm South Equatorial Belt (SEB, 16°S - 6°S). Figure 4 shows that the CH_3D features are considerably narrower in the EqZ than they are in the SEB.

This difference was further explored by performing retrievals with the NEMESIS retrieval algorithm. Based on the conclusion of Section 4, we initially assumed a cloud structure made up of a single compact cloud layer at 0.8 bar, with scattering properties $\omega = 0.9$ and $g = 0.8$. The optical thickness of this cloud was allowed to vary, along with the abundances of the molecular species as described in Section 3. For the SEB, the retrieved CH_3D abundance was 0.15 ppm, approximately the same as the value obtained by Lellouch et al. (2001). However, the EqZ produced a much lower value of 0.09 ppm.

As a further test, additional retrievals were run where the EqZ CH_3D abundance was fixed to the higher level and the SEB abundance was fixed to the lower level. The results of this are shown by the coloured lines in Figure 4 and they show that the EqZ and the SEB cannot be fit using the same CH_3D abundance. A VMR of 0.15 ppm fits the SEB data, but is too broad for the EqZ data, and a VMR of 0.09 ppm fits the EqZ data but is too narrow for the SEB.

However, a factor ~ 2 difference in CH_3D abundance for different regions of the planet is not physically plausible.

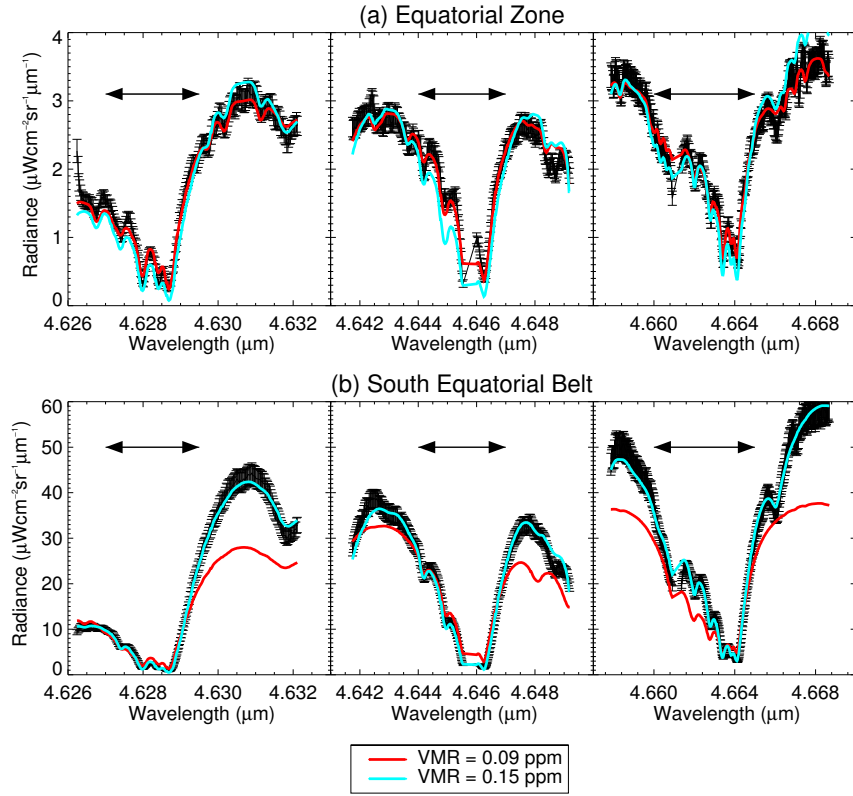


Figure 4: CH_3D absorption feature fits in two different regions of the planet. CRIREs data is shown in black, and the CH_3D features are shown by the horizontal arrows. Each colour shows the fit obtained using different CH_3D abundances: 0.09 ppm (the best fit value for the EqZ) and 0.15 ppm (the best fit value for the SEB).

As described in the previous section, methane and its isotopologues are expected to be well-mixed in the troposphere, with no spatial variability. We must therefore consider an alternative explanation for this change in CH₃D lineshape.

5.2.2. Deep cloud structure

One possibility is spatial variability in the deep cloud structure. As described by Bjoraker et al. (2015), this can be modelled by considering the presence of deep clouds at the pressure levels where water is expected to condense (~ 5 bar). If there is very little cloud opacity at these pressures, the radiation is originating from deep in the atmosphere, where the pressure is higher. Pressure broadening therefore leads to a lineshape with broad wings. Inserting an optically thick cloud layer at 5 bar has two effects on the spectrum: (i) it reduces the continuum radiance, decreasing the apparent depth of the absorption feature and (ii) it moves the weighting function upwards to a region of lower pressures and cooler temperatures, leading to a narrower lineshape.

Since the presence of a deep cloud can act to narrow the lineshape, this suggests that we may be able to fit the narrow EqZ absorption features while keeping the CH₃D abundance fixed at the retrieved value for the SEB. To test this we inserted a deep cloud deck at 5 bar. We assumed the same simple properties as the upper cloud: compact, spectrally flat, $\omega = 0.9$ and $g = 0.8$. We then performed a retrieval where the opacity of this deep cloud was allowed to vary. The CH₃D abundance was held fixed at 0.149 ppm and, as before, the upper cloud and other gaseous species were also allowed to vary. The results are shown by the yellow line in Figure 5. For comparison, we also show the case where there is no deep cloud in blue (identical to the blue line in Figure 4a).

The comparison between the blue and yellow lines shows that this addition considerably improves the fit. The retrieved deep cloud opacity in the EqZ is 230, making the cloud essentially opaque. This agrees with Bjoraker et al. (2015), where the deep cloud in the EqZ was assumed to be opaque. As with Bjoraker et al. (2015), this shows that the difference in CH₃D lineshape between the EqZ and the SEB can be accounted for by the variations in the deep cloud structure; the deep cloud is transparent in the SEB and opaque in the EqZ.

Based on Bjoraker et al. (2015), the initial analysis was performed using an opaque cloud at 5 bar. We carried out further retrievals in order to test the sensitivity to the cloud location. If the cloud is placed too deep, it falls outside the pressure range probed by 5- μ m spectra, and can no longer influence the spectral shape. If the cloud is placed too high, it simply plays the same role as the original 0.8-bar cloud and so does not improve the fit. However, between these two extremes, we find that a broad range of cloud locations from 2 to 7 bar can provide a good fit to the data, with deeper pressure levels requiring higher

cloud opacities. In the absence of further constraint, we continue the analysis using the original 5 bar value.

5.2.3. Latitudinal retrieval

In the previous sections, we were just comparing two discrete parts of the planet, the EqZ and the SEB. We now extend that analysis to perform a full latitudinal retrieval of the deep cloud opacity, using the same CH₃D features as in the previous sections. Spectra were smoothed in the spatial direction with a width of 5 pixels in order to reduce the noise, and the sampling rate was 3 pixels. For each smoothed spectrum, we ran a retrieval following the same procedure as in Section 5.2.2. The retrieved cloud optical thicknesses are shown in Figure 6. In the belts, the retrieved deep cloud opacity is ~ 0.1 (relatively transparent), and for the zones the retrieved deep cloud opacity is ~ 100 (relatively opaque).

The absolute values of the both cloud optical thickness are very dependent on (i) the accuracy of the radiometric calibration, (ii) the cloud locations and (iii) the choice of cloud scattering parameters. The error bars shown in Figure 6 do not include these error sources. Changes to either of the first two factors result in a cloud opacity profile that is either scaled up or scaled down, but the relative shape of the latitudinal profile remains constant. The third factor can affect the relative shape of the latitudinal profile, as described in Section 5.2.4.

5.2.4. Sensitivity to the scattering parameters

Section 4 showed that decreasing the asymmetry parameter, g , can act to significantly increase the retrieved gaseous abundances in the cloudy parts of the planet while having a negligible effect on the abundances in the cloud-free regions. This therefore has the potential to solve the problem posed in Section 5.2.1 without having to invoke the presence of a deep cloud deck. With $g = 0.8$, the retrieved CH₃D abundance in the EqZ was 0.09 ppm, compared to 0.15 ppm in the SEB. If instead, we set $g = 0.4$, the EqZ abundance increases to 0.16, while the SEB abundance remains 0.15 ppm, removing the discrepancy between the two regions. This is shown further by Figure 7, which shows the same latitudinal cloud profiles as Figure 6 for the case where $g = 0.4$. Comparing these two figures shows that the change in scattering parameters significantly affects the latitudinal profile. The deep cloud is relatively transparent everywhere, with little difference between the belts and the zones. It is therefore clear that the conclusions about the existence of a cloud deck at 5 bar are fairly sensitive to the assumptions made about the scattering properties of the cloud deck at 0.8 bar.

5.3. Summary

In this section, we have shown that the shape of the CH₃D 5- μ m absorption features varies with latitude. We initially showed that this can be modelled in two different ways; either by allowing the CH₃D abundance to vary spatially, or by allowing the opacity of a 5-bar tropospheric

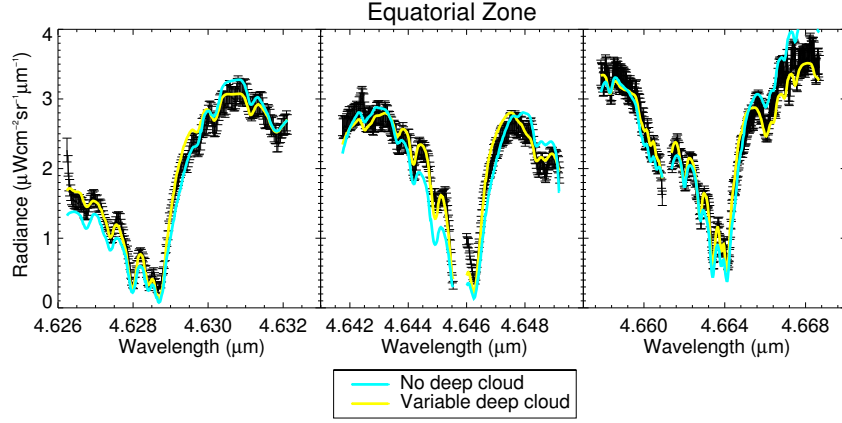


Figure 5: Retrievals of three CH_3D features in the cool EqZ, with varying the cloud structure. The blue line shows the best fit when there is no deep cloud present, and the yellow line shows the fit where the opacity of a deep cloud at 5 bar is allowed to vary. In both cases, the CH_3D abundance is fixed at 0.16 ppm.

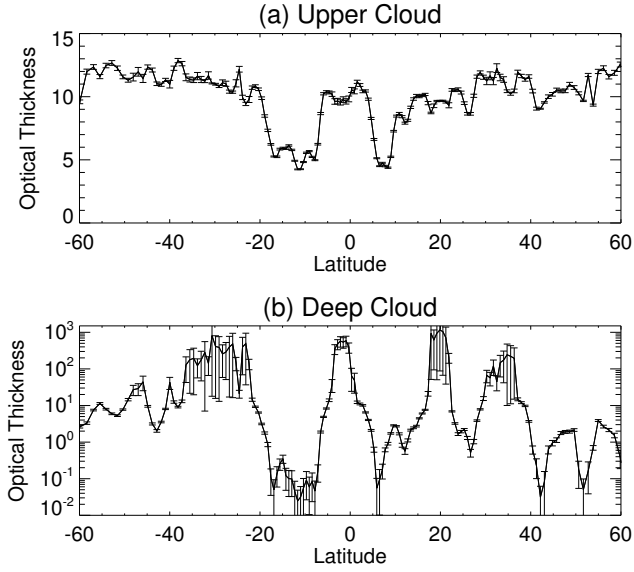


Figure 6: Retrieved cloud optical thicknesses as a function of latitude. The retrievals show that the cool zones are fit using an opaque deep cloud, while the warm belts are fit using an optically thin deep cloud.

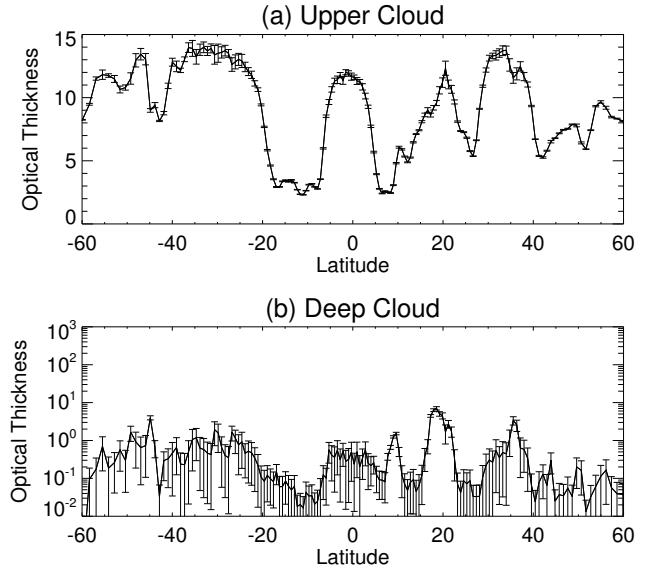


Figure 7: Retrieved cloud optical thicknesses as a function of latitude, using $g = 0.4$ instead of $g = 0.8$ for the upper cloud.

cloud to vary. We ruled out the former option on the grounds that CH_3D should have a constant VMR throughout the troposphere, so we therefore accept the latter option. This suggests that there is an optically thick deep cloud layer present in the EqZ. We then performed a full latitudinal retrieval, where the opacity of this deep cloud was independently retrieved at each latitude, and we found that the deep cloud is opaque in the zones and transparent in the belts.

It should be noted, however, that these conclusions are sensitive to the scattering properties of the upper cloud deck. The above conclusions are based on an asymmetry parameter of $g = 0.8$, which was the best-fit value found in Section 4. However, if the asymmetry parameter is reduced to $g = 0.4$, then the conclusions about the presence of a deep cloud are no longer valid. While $g = 0.8$ did produce a better fit to the data than $g = 0.4$, a value of 0.4 is still within a plausible range of values. We therefore conclude that while there is some evidence for the presence of a deep cloud, it is weakened by the degeneracies with the cloud scattering properties.

6. GeH_4

6.1. Introduction

Germane (GeH_4) is a molecular species that only exists in thermochemical equilibrium deep in Jupiter’s atmosphere (Taylor et al., 2004). In the 298–2000 K range, GeH_4 is modelled to be the second most abundant Ge species (after GeS), but as the altitude increases and the temperature decreases, it is destroyed in favour of either GeS or GeSe (Fegley and Lodders, 1994). Because of this, GeH_4 was not expected to be present in observable quantities in the upper troposphere at the pressure levels that are probed by the majority of the infrared spectrum. However, the 5- μm atmospheric window probes much deeper into the atmosphere, leading Corice and Fox (1972) to predict that GeH_4 absorption features might be visible in this part of the spectrum.

GeH_4 has two infrared active fundamental bands, ν_3 (4.737 μm) and ν_4 (12.210 μm). Fortunately, ν_3 is located in the middle of the 5- μm window, providing the perfect opportunity to detect the disequilibrium species. It was the Q-branch of the ν_3 fundamental that was first identified as a jovian GeH_4 feature by Fink et al. (1978), using observations from the Kuiper Airborne Observatory (KAO). They derived a tropospheric GeH_4 abundance of 0.6 ppb. The same spectral feature was subsequently observed in data from the Infrared Interferometer Spectrometer (IRIS) on the Voyager 1 spacecraft (Kunde et al., 1982; Drossart et al., 1982). Using new observations from KAO, Bjoraker et al. (1986) identified additional GeH_4 features, corresponding to the R3 and R6 transitions. In addition, they identified the Q-branch of the ν_1 fundamental at 4.738 μm ; although this band is ‘forbidden’ under symmetry considerations, weak absorption lines were identified in laboratory spectra by Lepage et al. (1981).

For these earlier analyses, the available spectroscopic data was restricted to a single isotopic species, $^{74}\text{GeH}_4$. In fact, there are five naturally occurring isotopes of germanium: ^{70}Ge , ^{72}Ge , ^{73}Ge , ^{74}Ge and ^{76}Ge . The terrestrial relative abundances are 20.6%, 27.5%, 7.8%, 36.5% and 7.7% respectively (Berglund and Wieser, 2011).

Bézard et al. (2002) was the first study to include line data for all five isotopic species of GeH_4 . They used theoretical line data which they scaled to match observations for a single isotope, and assumed telluric relative abundances. Their derived VMR of 0.45 ppb was 35–50% lower than previous estimates, which they attributed to the use of the additional isotopes. We take a similar approach to the GeH_4 line data as Bézard et al. (2002). We generated theoretical line lists for each isotope using the Spherical Top Data System (Wenger and Champion, 1998), and then scaled these to match the observed $^{74}\text{GeH}_4$ data from the GEISA database (Jacquinot-Husson et al., 1999). We also assume telluric relative abundances. As in previous studies, we assume that GeH_4 is well-mixed in the troposphere.

Previous studies of GeH_4 have generally been restricted to a single region of the planet: either an average over the centre of the disc (Fink et al., 1978; Bjoraker et al., 1986) or a focus on the bright NEB (Kunde et al., 1982; Bézard et al., 2002). The exception to this is Drossart et al. (1982), who found that within a factor of 2, the same GeH_4 abundance was able to fit the range of spectra from 30°S to 30°N. We use the improved spectral resolution afforded by CRIRES to repeat this latitudinal study and to extend it to higher latitudes.

6.2. Analysis

6.2.1. Identification of GeH_4 features

Our first task is to identify the GeH_4 absorption features in the 5- μm spectra. Based on previous studies, we know that there is a strong Q-branch feature at 4.737 μm . In a preliminary investigation, we determined that this absorption feature was particularly clear in the bright SEB; we therefore used this spatial region in order to search for additional GeH_4 absorption features.

The identifiable GeH_4 absorption features in the CRIRES spectra are shown in Figure 8. The NEMESIS retrieval algorithm was used to model the data, and the best-fit is shown in red. In order to highlight the shape and location of the GeH_4 absorption features, the blue line shows what the spectrum would look like in the absence of GeH_4 . Each feature is labelled, and is comprised of a blend of the five isotopologues.

The Q, R3 and R6 bands have been identified in previous studies (Fink et al., 1978; Bjoraker et al., 1986). In addition, we identify the R7 line, located at 4.639 μm . From each of these four spectral features, we retrieve the following GeH_4 abundances: 0.51 ppb (R7), 0.62 ppb (R6), 0.45 ppb (R3), 0.58 ppb (Q). These small differences could reflect genuine differences, due to each line probing a slightly different pressure level, or they could be due to inaccuracies in the line data. As each segment was observed at a

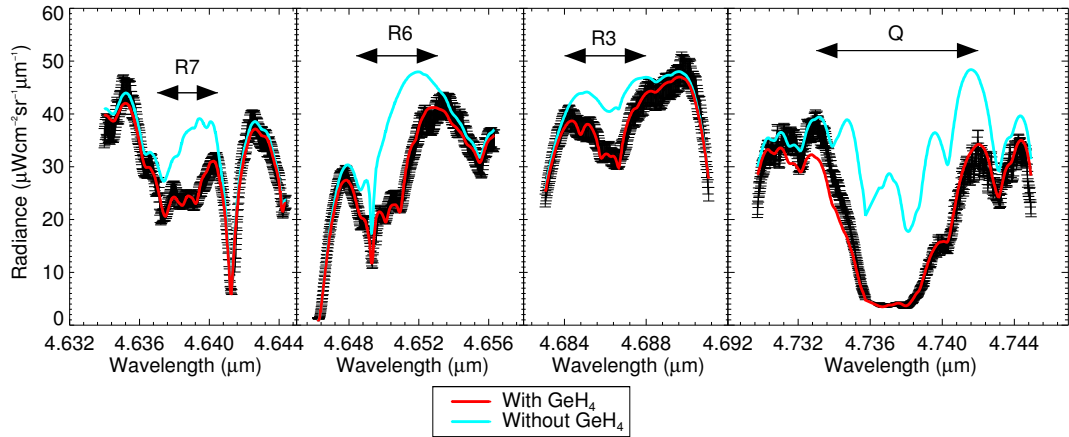


Figure 8: Identification of GeH_4 absorption features in the 5- μm window. CRIRCS data is shown in black and is taken from the SEB. The best fits obtained from two retrievals are shown: with GeH_4 present (red) and with no GeH_4 present (blue).

different time, and therefore a different longitude, a simultaneous retrieval of all four features is not possible.

6.2.2. Spatial variability

Having identified GeH_4 absorption features in one discrete region of the planet (the SEB), we now consider how this varies with latitude. We will focus on the most prominent GeH_4 feature, the Q-branch at 4.734–4.742 μm .

Figure 9 shows the same absorption feature for three different regions of the planet: the EqZ, the SEB and a “Northern Region”, corresponding to 50–55°N. Comparing the data, shown in black, from the three regions highlights some differences: the absorption feature appears to be deepest in the SEB and shallowest in the EqZ. This would appear to suggest that there is less GeH_4 present in the EqZ. However, the previous sections have already demonstrated a degeneracy between cloud properties and retrieved gaseous abundances. Section 4 showed that the depth of an absorption feature can depend on the scattering properties of the main cloud deck, and Section 5 showed that it can also depend on the presence/absence of a deep cloud deck. Since the primary difference in line shape is between the EqZ and SEB, which we expect to have very different cloud structures, it is likely that clouds play an important role.

In order to explore whether or not the CRIRCS observations provide evidence for spatial variability in GeH_4 , we performed a series of retrievals on these three spectra, making different assumptions about the cloud structure. The red line shows the case where there is a single upper cloud deck, with an asymmetry parameter $g = 0.8$. The retrieved GeH_4 abundances are 0.19 ppb (EqZ), 0.58 ppb (SEB) and 0.44 ppb (Northern Region); in this case, the shallow feature in the EqZ does indeed lead to a lower retrieved abundance.

The yellow line in Figure 9 shows the case where the

asymmetry parameter of the cloud is changed to 0.4. Because the SEB and Northern Region have low optical thicknesses, this has a negligible effect of those retrievals (now 0.59 ppb and 0.47 ppb respectively). There is a significant effect for the EqZ, increasing the retrieved abundance from 0.19 ppb to 0.47 ppb. Changing the asymmetry parameter (i.e. making the cloud particles less forward scattering) can therefore account for much of the apparent difference between the EqZ and the SEB.

Alternatively, the difference can be accounted for by the presence/absence of a deep cloud. In Section 5, we fixed the CH_3D abundance to the SEB value, and we were able to fit the EqZ by adding a deeper cloud deck. We repeat the same process here: upper cloud is returned to an asymmetry parameter of 0.8, the GeH_4 abundance is fixed to the SEB value (0.58 ppb) and the opacity of a deep cloud at 5 bar is allowed to vary in the retrievals. The green line in Figure 9 shows the fits obtained for this case. The retrieved deep cloud is opaque in the EqZ and transparent in the SEB, just as in Section 5. This shows that the deep cloud structure studied in Section 5 can account for the difference in line shape between the EqZ and SEB.

6.2.3. Latitudinal retrieval

Section 6.2.2 showed that there is no evidence for spatial variability in GeH_4 between three discrete regions of the planet, as any differences in line shape can be accounted for by changes in the cloud structure alone. In this section, we extend the analysis to cover the full range of latitudes available. Figure 10 shows the GeH_4 abundance as a function of latitude, retrieved with different assumptions. Alongside this is the goodness-of-fit (χ^2/n), which describes the quality of the fit at each latitude point. As with Figure 9, the three colours correspond to different assumptions made in the retrievals.

The red line corresponds to the simplest case, where

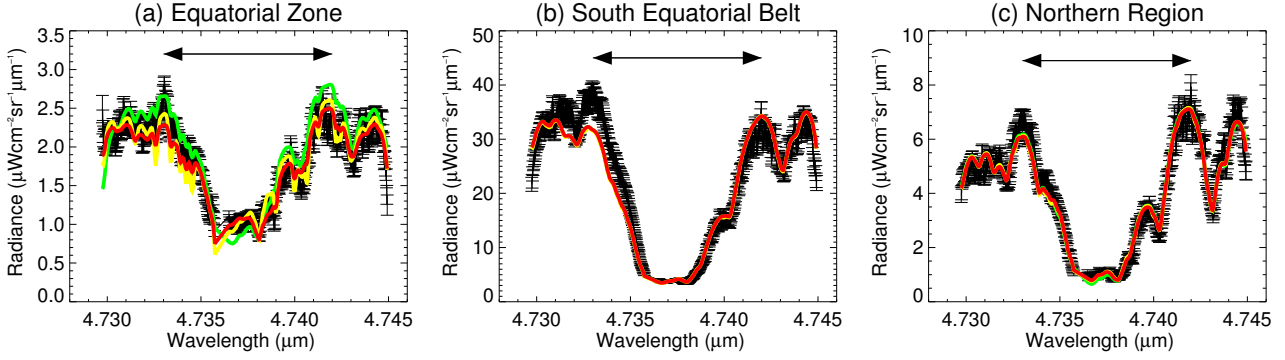


Figure 9: GeH_4 absorption feature fits in the Equatorial Zone and South Equatorial Belt. The CRIREs observations are shown in black. The coloured lines show the best fit that can be achieved using different assumptions. Red: single cloud deck with $g = 0.8$, GeH_4 allowed to vary. Yellow: single cloud deck with $g = 0.4$, GeH_4 allowed to vary. Green: upper cloud deck with $g = 0.8$, additional deep cloud deck, GeH_4 held fixed.

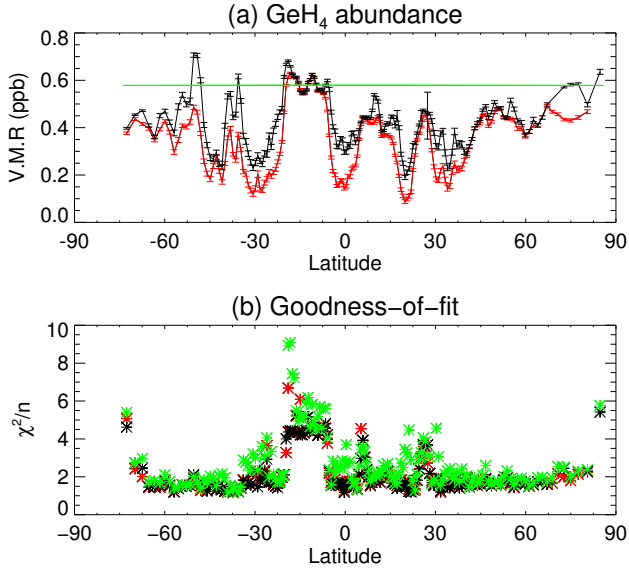


Figure 10: GeH_4 abundance and goodness-of-fit values as a function of latitude, for three different assumptions. Red: single cloud deck with $g = 0.8$, GeH_4 allowed to vary. Black: additional deep cloud deck with opacities derived from Section 5, GeH_4 allowed to vary. Green: deep cloud deck allowed to vary, GeH_4 held fixed at 0.58 ppb.

there is a single upper cloud deck (with $g = 0.8$) and the GeH_4 abundance is allowed to vary, i.e. the same as the red line in Figure 9. Section 6.2.2 showed that this simple case led to a variability in the retrieved GeH_4 abundance, with a depletion in the EqZ and an enhancement in the SEB. Figure 10 shows that this applies at all latitudes, and so this simple assumption leads to an apparent belt-zone variability.

The black line corresponds to the case where an additional deep cloud is included in the model and its latitudinal profile is fixed to the values retrieved in Section 5 (shown in Figure 6). It should be noted that this previously determined deep cloud latitudinal profile relates to a different longitude, so it is not necessarily expected to be identical to the cloud profile at this longitude. Nevertheless, the overall latitudinal trend is likely to be very similar and it provides an insight into the role of the deep cloud on the retrieved abundances. Once again, the GeH_4 abundance is allowed to vary in the retrievals. It can be seen in Figure 10a that the presence of this deep cloud increases the retrieved abundances in the zones, decreasing the apparent belt-zone variability shown by the red line. Figure 10b shows that this change does not alter the quality of the fits.

For the green line, the GeH_4 abundance is held fixed as a function of latitude and the opacity of the deep cloud is allowed to vary, instead of being held fixed at the values determined in Section 5. This is the same as the green lines in Figure 9. As in Section 6.2.2, the GeH_4 abundance chosen is the best-fit value from the SEB (0.58 ppb). Since the SEB is relatively cloud-free, there are no complications from the cloud structure and this should represent the ‘true’ abundance. The goodness-of-fit in Figure 10 shows that this constant abundance is able to provide a similar fit to the data at all latitudes. Section 6.2.2 previously showed that variability in the deep cloud opacity could account for the difference in line shape between three discrete regions of the planet, and Figure 10 shows that

this remains true across the full range of latitudes.

6.3. Summary

In this section, we have identified four GeH_4 absorption features in the CRIRES observations, one of which has not been previously identified. Using the strongest absorption feature, we searched for latitudinal variability and found that there are some differences in the line depth between the EqZ, the SEB and the Northern Region of the planet. However, this difference in line shape does not necessarily indicate a difference in the abundance of GeH_4 . We found that the variation in line shape could be accounted for by Jupiter’s tropospheric cloud structure. This analysis was then extended to all latitudes, and it was found that a single fixed GeH_4 abundance could be used to fit all spectra without compromising the quality of the fits. The CRIRES observations therefore do not provide any evidence for spatial variability in GeH_4 . This highlights the high level of degeneracy present in the problem. The deep cloud structure, which has not been included in any previous studies of GeH_4 , significantly complicates the analysis.

7. AsH_3

7.1. Introduction

Arsine (AsH_3) is the most abundant arsenic gas on Jupiter. Deep in the atmosphere it exists in thermochemical equilibrium but, in the absence of vertical motion, it precipitates into $\text{As}_4(\text{s})$ or $\text{As}_2\text{S}_2(\text{s})$ at ~ 400 K (Fegley and Lodders, 1994). As with GeH_4 , this means that the $5\text{-}\mu\text{m}$ atmospheric window is an ideal spectral region to search for the species.

AsH_3 has two fundamental bands within the $5\text{-}\mu\text{m}$ window: ν_1 at $4.728\text{ }\mu\text{m}$ and ν_3 at $4.704\text{ }\mu\text{m}$. Of these, the ν_3 band is stronger and its Q-branch led to the first detection of AsH_3 on Jupiter by Noll et al. (1989), using spectra obtained from the United Kingdom Infrared Telescope. They initially estimated the deep molar abundance to be $0.7^{+0.7}_{-0.4}$ ppb, which was then revised down to 0.22 ± 0.11 ppb the following year, after acquisition of new airborne and ground-based spectra and additional laboratory line data (Noll et al., 1990). More recently, Bézard et al. (2002) used data from the Canada-France-Hawaii Telescope to obtain an abundance of 0.24 ppb. The Q-branch of the ν_3 band remains the only AsH_3 feature to have been identified on Jupiter; we will search for evidence of additional AsH_3 absorption lines. As with GeH_4 , we assume that AsH_3 is well-mixed in the troposphere.

Out of the previous studies of AsH_3 , only Noll et al. (1990) studied more than one region of the planet. They made observations of both the EqZ and the NEB and found that these spectra matched to within the noise levels. As the CRIRES observations provide both high spectral resolution and high spatial resolution, we will extend this analysis to cover all latitudes.

7.2. Analysis

7.2.1. Identification of AsH_3 features

As with GeH_4 , we first seek to simply identify the AsH_3 absorption features in the $5\text{-}\mu\text{m}$ spectrum. The only previously identified feature is the Q-branch at $4.704\text{ }\mu\text{m}$; in a preliminary investigation we determined that this feature was particularly strong at high latitudes ($50\text{-}55^\circ\text{N}$) so we use this ‘Northern Region’ in order to search for additional absorption lines.

We were able to identify two additional absorption features, corresponding to the R1 and P6 lines of the ν_3 band (Dana et al., 1993). These lines are shown in Figure 11, alongside the Q-branch. The CRIRES data is shown in black. The blue lines show the best fit that can be achieved when no AsH_3 is present in the atmosphere and the red lines show the best fit that can be achieved when the AsH_3 abundance is allowed to vary. As in Section 6.2.1, the cloud opacity of the single cloud deck and the gaseous abundances were also allowed to vary. In each case, the addition of AsH_3 significantly improves the fit. We obtain the following abundances from each retrieval: 0.60 ppb (R1), 0.49 ppb (Q) and 0.46 ppb (P6).

7.2.2. Spatial variability

We now consider how the AsH_3 lineshape varies with latitude, and how this affects the retrieved abundances. As in previous studies, we focus on the most prominent AsH_3 absorption feature in the $5\text{-}\mu\text{m}$ window, the Q-branch of the ν_3 fundamental, located at $4.704\text{ }\mu\text{m}$. Figure 12 shows this spectral region for the three regions of the planet considered in Section 6. Unlike the previous GeH_4 section, the EqZ and the SEB have similar spectral shapes. In this case, however, there is significant variation between these spectra and the spectrum from the Northern Region. The absorption feature at $4.704\text{ }\mu\text{m}$ is considerably flatter in Northern Region than it is in the SEB and the EqZ, suggesting a higher abundance of AsH_3 at high latitudes.

This is confirmed by a simple NEMESIS retrieval, shown in red in Figure 12. This fit is analogous to the red line in Figure 9, where the cloud structure consists of a single upper cloud with $g = 0.8$. With these assumptions, we obtain the following retrieved abundances for AsH_3 : 0.01 ppb in the EqZ, 0.02 ppb in the SEB and 0.49 ppb in the Northern Region. In the case of the EqZ and the SEB, the retrieved abundances are so low that they are essentially zero.

In Section 6, we found that the apparent change in GeH_4 lineshape could be accounted for by variations in the cloud structure, rather than changes in the GeH_4 abundance itself. However, clouds are unlikely to be responsible here, since the EqZ and the SEB have very different cloud structures, and yet the AsH_3 features have similar spectral shapes. The observed effect is also unlikely to be due to limb darkening at high altitudes. Firstly, previous studies have shown that Jupiter’s tropospheric clouds are highly scattering, which minimises the effect of limb darkening (Roos-Serote and Irwin, 2006; Giles et al., 2015).

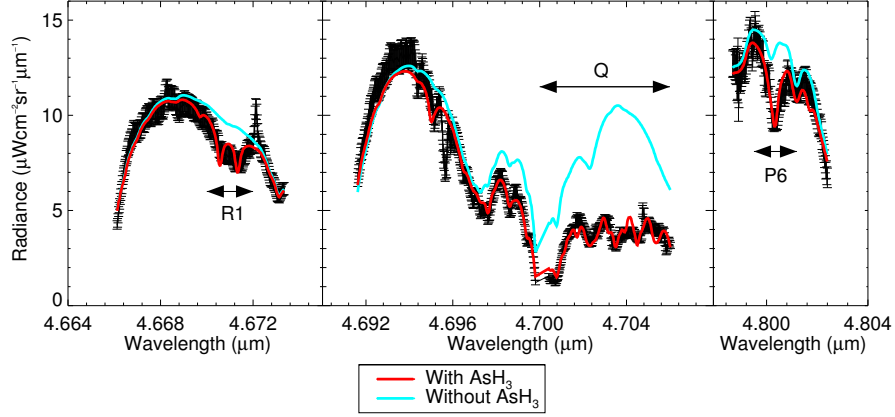


Figure 11: Identification of AsH_3 absorption features in the 5- μm window. CRIRES data is shown in black, and is taken from the Northern Region of the planet. The best fits obtained from two retrievals are shown: with AsH_3 present (red) and with no AsH_3 present (blue).

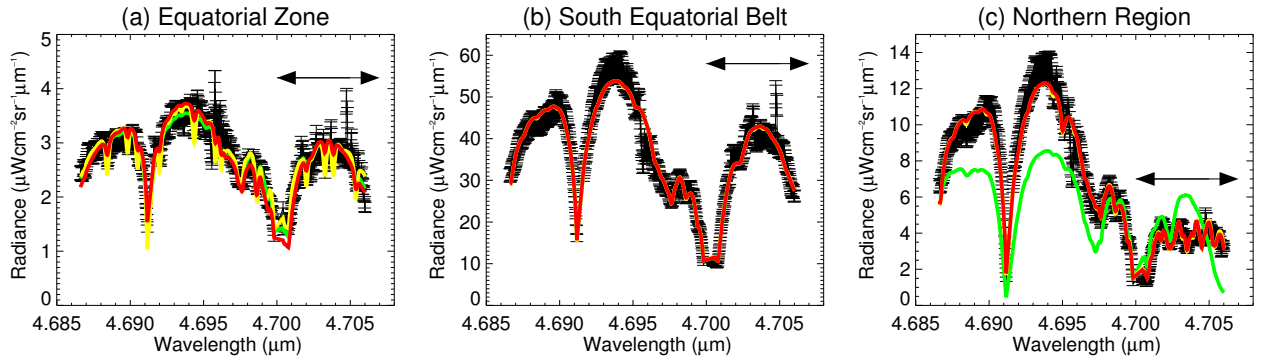


Figure 12: AsH_3 absorption feature fits at different latitudes. The CRIRES observations are shown in black. The coloured lines show the best fit that can be achieved using different assumptions. Red: single cloud deck with $g = 0.8$, AsH_3 allowed to vary. Yellow: single cloud deck with $g = 0.4$, AsH_3 allowed to vary. Green: upper cloud deck with $g = 0.8$, additional deep cloud deck, AsH_3 held fixed.

Secondly, even if there was a significant limb darkening effect, we would see the opposite phenomenon. As we move to higher latitudes, the emission angle increases, and we therefore probe higher in the atmosphere, where (as a disequilibrium species) AsH_3 is *less* abundant, not more.

Nevertheless, in order to fully explore any degeneracy, we repeated the different retrievals performed in Section 6. The yellow line in Figure 12 shows the fits that are obtained when the asymmetry parameter of the upper cloud is changed from 0.8 to 0.4. The retrieved abundance in the EqZ is increased from 0.01 ppb to 0.05 ppb, and the SEB and Northern abundances remain essentially unchanged at 0.02 ppb and 0.50 ppb respectively. We are unable to close the gap between the equatorial regions and the high latitudes by changing the scattering properties of the upper cloud.

We then consider the effect of a deep cloud. The AsH_3 were held constant at the SEB level (0.02 ppb) and the opacity of a deep cloud was allowed to vary. The results are shown by the green line in Figure 12. As in Section 6, the EqZ and SEB can be fit using the same AsH_3 abundance, provided that the deep cloud is optically thick in the EqZ. However, it is clear from Figure 12(c) that this constant abundance cannot be applied to the Northern Region of the planet. We therefore conclude that the spatial variation in the AsH_3 lineshape is indicative of genuine latitudinal variability in the abundance of AsH_3 .

7.2.3. Latitudinal retrieval

Having established that there is evidence for spatial variability in AsH_3 , we now extend the analysis from three discrete sections to a full latitudinal retrieval of AsH_3 . Figure 13 shows the latitudinal distribution of AsH_3 alongside the goodness-of-fit values. The three different colours correspond to the same assumptions described in Section 6.2.3.

For the latitudinal distribution shown by the red line, there is a single upper cloud deck with $g = 0.8$ and the AsH_3 abundance is allowed to vary, i.e. the same as the red line in Figure 12. Section 7.2.2 showed that this simple case produced similar retrieved abundances in the EqZ and SEB and an enhanced abundance in the Northern Region. This pattern is confirmed by the full latitudinal retrieval; there is a roughly symmetrical distribution, with an increased abundance at high latitudes.

The black line shows the case where an additional deep cloud is included in the model, with the latitudinal profile obtained from Section 5. While the precise values of the retrieved abundances do change slightly with the inclusion of this additional cloud deck, the overall trend of an enhancement at high latitudes remains true. The errors shown in Figure 13 represent the formal errors on the retrieval; the difference between the red and black lines shows that these formal errors are significantly smaller than the errors due to varying assumptions about cloud structure. As with Section 6.2.3 for GeH_4 , the inclusion of an additional cloud does not alter the quality of the fits.

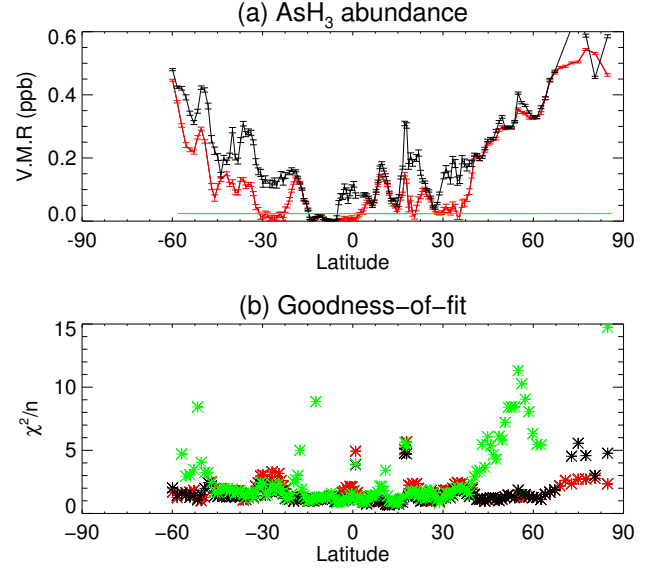


Figure 13: AsH_3 abundance and goodness-of-fit values as a function of latitude, for three different assumptions. Red: single cloud deck with $g = 0.8$, AsH_3 allowed to vary. Black: additional deep cloud deck with opacities derived from Section 5, AsH_3 allowed to vary. Green: deep cloud deck allowed to vary, AsH_3 held fixed at 0.02 ppb.

This is in contrast to the final case, shown by the green line. In this case, the AsH_3 abundance is held fixed at the SEB value of 0.02 ppb and the deep cloud is allowed to vary. Section 7.2.2 showed that this can provide a good fit in the EqZ and SEB, but fails to provide a good fit for the Northern Region. Figure 13 extends this to all latitudes and shows that this constant abundance can provide a good fit between 40°S and 40°N , i.e. there is no evidence for belt-zone variability. However, the fit worsens considerably at high latitudes; an abundance of 0.02 ppb simply cannot fit these regions, regardless of the opacity of the deep cloud. This leads to the conclusion that there is a genuine enhancement at high latitudes.

Figure 13 is restricted to the data from 12 November 2012. However, Figure 14 shows that the 1 January 2013 dataset produces consistent results, and that the overall conclusion of an AsH_3 enhancement at high latitudes is reproducible.

7.3. Summary

In this section, we have identified three AsH_3 absorption features in the CRIRES observations, two of which have not been previously identified. Using the strongest absorption feature, we searched for latitudinal variability and found that there are significant differences in the line shape between spectra from the equatorial regions (EqZ and SEB) and spectra from the far northern latitudes. These differences cannot be accounted for by Jupiter's cloud structure, and we therefore conclude that there is evidence for latitudinal variability in the abundance of AsH_3 .

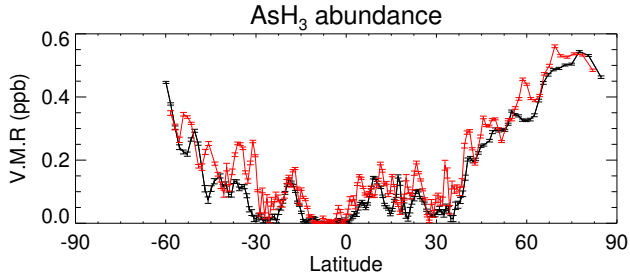


Figure 14: AsH_3 abundance as a function of latitude from the 12 November 2012 dataset (black) and the 1 January 2013 dataset (red). In both cases, a single cloud deck with $g = 0.8$ is assumed and the AsH_3 abundance is allowed to vary. The two datasets produce consistent results.

This was further shown by a latitudinal retrieval, which demonstrated that a constant AsH_3 abundance is inconsistent with the observations. Instead, the retrieved AsH_3 abundances have a roughly symmetrical latitudinal profile, with a minimum in the equatorial regions and enhanced abundances at high latitudes.

8. PH_3

8.1. Introduction

Like GeH_4 and AsH_3 , phosphine (PH_3) is a disequilibrium species in Jupiter's troposphere. Deep in the atmosphere it is the primary phosphorus gas but at higher altitudes thermal decomposition produces PH, which then reacts with OH radicals to form P_4O_6 (Fegley and Lodders, 1994). However, the solar abundance of P is much greater than the solar abundances of Ge or As (Grevesse et al., 2007). This means that even though the VMR of PH_3 decreases rapidly with altitude, it is still present in observable quantities in the upper troposphere and is therefore detectable outside the $5\text{-}\mu\text{m}$ window.

Strong PH_3 absorption features can be seen at $\sim 5\text{ }\mu\text{m}$ and at $\sim 10\text{ }\mu\text{m}$. PH_3 was simultaneously detected in both of these spectral regions. Ridgway et al. (1976) noted that including a solar abundance of PH_3 in their model improved their fit to $10\text{-}\mu\text{m}$ observations of Jupiter from the McMath Solar Observatory. This was then confirmed by Larson et al. (1977), who also found that a roughly solar abundance of PH_3 was able to fit their $5\text{-}\mu\text{m}$ airborne observations.

The $5\text{-}\mu\text{m}$ and $10\text{-}\mu\text{m}$ spectral regions probe different pressure levels in Jupiter's troposphere. At $5\text{-}\mu\text{m}$, the spectrum is primarily sensitive to the lower troposphere ($p > 1$ bar) whereas the $10\text{-}\mu\text{m}$ observations are mostly sensitive to the upper troposphere, at pressures $p < 1$ bar. This pressure difference allows us to start to constrain the vertical profile of PH_3 . Fletcher et al. (2009) modelled Jupiter's PH_3 abundance using a constant abundance of 1.86 ppm up to 1 bar, above which it drops off with a constant fractional scale height of 0.3. In this section, we will vary this

profile via a single scaling parameter; because the CRIRES data is from the $5\text{-}\mu\text{m}$ region, we are probing the deep abundance.

Several previous studies have also considered the possibility of spatial variability in the deep PH_3 abundance, as observed in the $5\text{-}\mu\text{m}$ window. Drossart et al. (1982) and Lellouch et al. (1989) searched for a correlation between cloud opacity and PH_3 abundance, but did not find any evidence. More recently, Drossart et al. (1990) and Giles et al. (2015) found evidence for a PH_3 enhancement at high latitudes compared to equatorial- and mid-latitudes. The spatially resolved $10\text{-}\mu\text{m}$ studies show a different pattern; the retrieved fractional scale height shows a global maximum over the equator and global minima at the NEB and SEB (Irwin et al., 2004; Fletcher et al., 2009).

8.2. Analysis

8.2.1. Spatial variability

For GeH_4 and AsH_3 , the choice of spectral region was clear, as there were very few absorption features in the $5\text{-}\mu\text{m}$ window. In contrast, PH_3 is one of the primary absorbers at $5\text{-}\mu\text{m}$, and there are many absorption features. In particular, the short-wavelength part of the $5\text{-}\mu\text{m}$ spectrum ($4.50\text{-}5.00\text{ }\mu\text{m}$) is dominated by PH_3 absorption. This might sound ideal, but in fact this prevents the accurate retrieval of PH_3 , as it becomes difficult to distinguish between PH_3 and other broad features such as the cloud opacity and the water vapour abundance. Instead, we look towards the long-wavelength edge, where PH_3 absorption contributes less to the continuum. We find that there is a clear, well-separated absorption feature at $5.071\text{ }\mu\text{m}$ and we will use this as the basis of our study of the deep PH_3 abundance in the troposphere.

Figure 15 shows this absorption feature for the same three spatial regions used in Sections 6 and 7. The CRIRES spectra in Figure 15 show variation in the depth of the PH_3 absorption feature; the feature is considerably deeper in the Northern Region than in the EqZ, while the SEB spectrum is between these two extremes.

The coloured lines show the best fit obtained for each spectrum, with the same assumptions as in Sections 6 and 7: the red line shows the case where there is a single upper cloud with $g = 0.8$ and the yellow line shows the case where there is a single upper cloud with $g = 0.4$. In the first case (red), the retrieved abundances in the EqZ, SEB and Northern Region are 0.49 ppm, 0.76 ppm and 1.22 ppm respectively. In the second case (yellow), these become 0.81 ppm, 0.75 ppm and 1.21 ppm. As in Section 7, altering the scattering properties of the cloud can account for the discrepancy between the EqZ and the SEB but not between the equatorial regions and the polar regions.

The green line in Figure 15 shows the case where the upper cloud has $g = 0.8$, the PH_3 abundance is fixed to the SEB value and the opacity of a second deep cloud

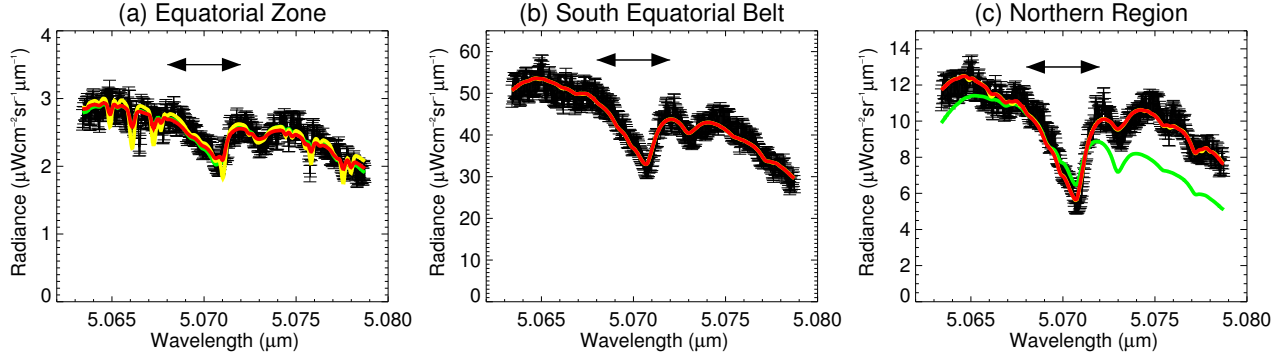


Figure 15: PH_3 feature fits at different latitudes. The CRILES observations are shown in black. The coloured lines show the best fit that can be achieved using different assumptions. Red: single cloud deck with $g = 0.8$, PH_3 allowed to vary. Yellow: single cloud deck with $g = 0.4$, PH_3 allowed to vary. Green: upper cloud deck with $g = 0.8$, additional deep cloud deck, PH_3 held fixed.

is allowed to vary. Again, the results are the same as for AsH_3 in Section 7. The presence of an optically thick deep cloud in the EqZ can account for the change in spectral shape between the EqZ and the SEB, but the same PH_3 abundance cannot be used to fit the regions at high latitude. We conclude that there is evidence for latitudinal variability in PH_3 .

8.2.2. Latitudinal retrieval

Having previously focussed on three discrete sections of the planet, we now turn to a full latitudinal retrieval of PH_3 . The results of these retrievals are shown in Figure 16; these results take the same form as Figure 10 (for GeH_4) and Figure 13 (for AsH_3) and the same conclusions can be drawn for PH_3 as for AsH_3 .

As with AsH_3 , the black and red lines in Figure 16 both show a polar enhancement in PH_3 , whether or not the additional deep cloud from Section 5 is included in the model. The case where the PH_3 abundance is held fixed at 0.76 ppm is shown in green, and this also follows the same pattern as AsH_3 ; at low latitudes, this model provides a good fit (i.e. there is no evidence for belt-zone variability), but the fit starts to worsen at high latitudes (in this case, above $\sim 60^\circ\text{N}$). This agrees with the conclusion made in Section 8.2.1 that there is evidence for an enhancement in PH_3 at high latitudes, with the retrieved abundance varying from ~ 0.5 ppm near the equator to 1.5 ppm at 80°N .

Figure 16 is restricted to the data from 12 November 2012. However, as with AsH_3 , the 1 January 2013 dataset produces consistent results (see Figure 17), showing that the overall conclusion of an PH_3 enhancement at high latitudes is reproducible.

8.3. Summary

In this section, we considered how the strength of a well-isolated PH_3 absorption line varied with latitude. We found that the depth of the absorption feature was greater

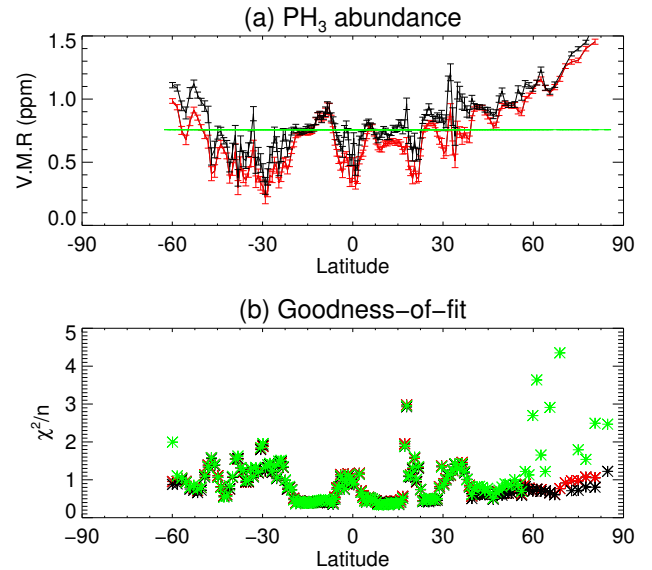


Figure 16: PH_3 abundance and goodness-of-fit values as a function of latitude, for three different assumptions. Red: single cloud deck with $g = 0.8$, PH_3 allowed to vary. Black: additional deep cloud deck with opacities derived from Section 5, PH_3 allowed to vary. Green: deep cloud deck allowed to vary, PH_3 held fixed at 0.76 ppm.

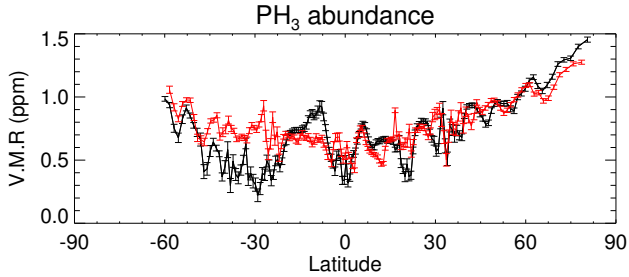


Figure 17: PH_3 abundance as a function of latitude from the 12 November 2012 dataset (black) and the 1 January 2013 dataset (red). In both cases, a single cloud deck with $g = 0.8$ is assumed and the AsH_3 abundance is allowed to vary. The two datasets produce consistent results.

for the high northern latitudes than for the equatorial latitudes. As with AsH_3 , we concluded that this was due to higher PH_3 abundances at high latitudes. We then performed a latitudinal retrieval, and found that this showed a minimum near the equator and an enhancement at high latitudes.

9. Discussion

9.1. Cloud structure and degeneracies

In Sections 4 and 5 we showed that there are significant degeneracies between Jupiter’s tropospheric clouds and the gaseous composition. Firstly, Section 4 showed that the retrieved abundances are sensitive to the cloud scattering properties; a high asymmetry parameter (more forward scattering, less reflected sunlight) leads to a low abundance, and a low asymmetry parameter (less forward scattering, more reflective sunlight) leads to a high abundance. The scattering properties also control the strength of the Fraunhofer lines in the spectrum, and by looking at the strength of these lines in the observations, we estimate that a value of $g = 0.8$ provides the best fit to the data. However, lower values can also provide an adequate fit, meaning that the degeneracy is not entirely broken.

Secondly, Section 5 showed that the deep cloud structure is also degenerate with the retrieved gaseous abundances. Increasing the optical thickness of a deep cloud has a similar effect on the spectrum as decreasing the molecular abundance. An optically thin deep cloud and a low abundance can produce a similar spectral shape to an optically thick cloud and a high abundance. In the case of CH_3D , this proves useful. The EqZ and SEB have different spectral shapes, yet we expect the CH_3D abundance to be constant. As described in Bjoraker et al. (2015), the presence of a cloud at 5 bar that is optically thick in the zones and optically thin in the belts can solve this ‘problem’. These observations therefore provide some evidence for the existence of a deep cloud; based on the location, this cloud is likely to be composed of water ice. However, the degeneracy with the scattering properties limits the

robustness of this conclusion. In the future, this could be improved by simultaneous modelling of the $5\text{-}\mu\text{m}$ region and the near-infrared reflected sunlight spectrum.

Both of these degeneracies complicate the retrievals of other molecular species. Since the cloud structure varies between belts and zones, these degeneracies especially limit our ability to come to reliable conclusions about belt-zone variability in gaseous abundances. This is further demonstrated in Section 6, where we showed that we were unable to distinguish between variability in GeH_4 abundance and variability in clouds.

9.2. Disequilibrium species

9.2.1. Abundances

In Sections 6-8, we measured the abundances of three disequilibrium species in Jupiter’s troposphere: GeH_4 , AsH_3 and PH_3 . For GeH_4 , we initially retrieved abundances that varied between 0.19 ppb (EqZ) and 0.58 ppb (SEB). By including a variable deep cloud, we were able to fit all spatial regions using a tropospheric abundance of 0.58 ppb. This is similar to previous results, which range from 0.45 ppb (Bézard et al., 2002) to 1.0 ppb (Drossart et al., 1982). This is significantly lower than the solar abundance of 6.7 ppb (Grevesse et al., 2007), but this is unsurprising as GeS , rather than GeH_4 , is the most abundant Ge species (Fegley and Lodders, 1994).

Unlike GeH_4 , measurements of the AsH_3 absorption feature showed evidence for an enhancement at high latitudes. Using a one-cloud model, the retrieved abundance varies from as low as 0.01 ppb in parts of the equatorial region to 0.55 ppb at 80°N . Previous measurements of the AsH_3 abundance have relied exclusively on data from the low latitudes of the planet, and have led to estimates of 0.2-0.3 ppb (Bézard et al., 1989; Noll et al., 1990; Bézard et al., 2002). Wang et al. (2016) notes that AsH_3 is expected to be the primary As gas in the troposphere, and that these previous studies therefore suggest that the jovian abundance of As is lower than the solar value (a solar abundance would lead to a volume mixing ratio of 0.34 ppb, Grevesse et al., 2007). This is surprising, as other heavy elements show an enrichment relative to solar abundances (e.g. Taylor et al., 2004). Our results show that in some parts of the planet, the observed AsH_3 abundance is subsolar, while in other regions, AsH_3 shows an enrichment of up to 1.6 times the solar value. It is possible that this higher abundance is more representative of the deep abundance of As.

As with AsH_3 , the retrieved PH_3 abundance varies with latitude, ranging from 0.5 ppm in the equatorial regions to 1.4 ppm at 80°N . These values are consistent with previous $5\text{-}\mu\text{m}$ observations of PH_3 : 0.7 ppm (Bjoraker et al., 1986), 0.77 ppm (Irwin et al., 1998) and 0.76-0.90 ppm (Giles et al., 2015). As noted in Giles et al. (2015), measurements at $5\text{-}\mu\text{m}$ appear to consistently lead to lower retrieved abundances than measurements at $10\text{-}\mu\text{m}$ (e.g. Fletcher et al., 2009); these differences are potentially due to errors in line data or cloud modelling uncertainties. Assuming a

solar abundance of P would lead to a volume mixing ratio of 0.43 ppm (Grevesse et al., 2007), so our analysis shows a variation from roughly solar levels to an enrichment of up to 3.3 times more the solar value, which is consistent with the observed enhancement of other heavy elements in Jupiter’s atmosphere.

9.2.2. Latitudinal profiles

In Sections 6-8, we studied the latitudinal distributions of GeH_4 , AsH_3 and PH_3 . We found no evidence for spatial variability in the abundance of GeH_4 . This result for GeH_4 agrees with the previous study of Drossart et al. (1982) who found no evidence for variability in the 30°S to 30°N region, and our analysis shows that this remains true at higher latitudes. This is in contrast to the results for AsH_3 and PH_3 . While there is no evidence for any belt/zone variability, both of these species exhibit an enhancement towards the poles. An enhancement at high latitudes has previously been reported for PH_3 (Drossart et al., 1990; Giles et al., 2015), but this is the first time that it has been seen in AsH_3 , as the only previous studies to compare different regions of the planet focussed exclusively on the equatorial latitudes (Noll et al., 1990).

Our results contrast with the theoretical predictions from Wang et al. (2016). In their work, they use a diffusion-kinetics code to investigate how the abundances of disequilibrium species in Jupiter’s troposphere depend on the vertical eddy diffusion coefficient, K_{eddy} . They find that GeH_4 has a different behaviour to AsH_3 and PH_3 , which agrees with our observations. The GeH_4 abundance is found to be very sensitive to the eddy diffusion coefficient, with a higher value of K_{eddy} leading to a higher tropospheric abundance. In contrast, PH_3 and AsH_3 do not appear to have any dependence on K_{eddy} (for a physically plausible range of K_{eddy}). These differences are due to the interplay between the quench level for the gas (the pressure at which the abundance is “frozen in”) and the equilibrium vertical profile. If the quench level is deep in the regime where the gas is well-mixed, then a small change in K_{eddy} will not alter the observed abundance. If the quench level is in a regime where the equilibrium abundance is rapidly changing with altitude, then a small change in K_{eddy} can have a significant effect on the observed abundance.

Wang et al. (2016) considers how abundances vary as a function of K_{eddy} , while a previous study by the same authors (Wang et al., 2015) looks at how K_{eddy} varies with latitude. In Wang et al. (2015), they suggest that rotation plays an increasingly important role in suppressing turbulent convection at higher latitudes and that K_{eddy} should decrease towards the poles. This also agrees with earlier theoretical work by Flasar and Gierasch (1978). Incorporating this finding, Wang et al. (2016) therefore predict that GeH_4 should decrease in abundance towards the poles, while AsH_3 and PH_3 should remain constant. In contrast, our observations show that GeH_4 is constant with latitude, while AsH_3 and PH_3 increase towards the poles.

It is unclear what the cause of this discrepancy is. One possibility is that it is due to photolytic destruction, which was not considered in Wang et al. (2016). Many studies have concluded that ultraviolet photons are a significant contribution to the destruction of PH_3 in the upper troposphere (e.g. Strobel, 1977; Ferris et al., 1984). It has also been suggested as a destruction mechanism for GeH_4 (Guillemin et al., 1995) and could plausibly apply to AsH_3 too. Geometry effects mean that higher latitudes receive fewer UV photons from the sun, and the higher opacity of stratospheric aerosols in the polar regions also acts as a shield to UV light (Zhang et al., 2013). Both of these effects could lead to a lower rate of photolytic destruction at high latitudes, and therefore a higher abundance. By increasing the abundances of all three species at high latitudes, the latitudinal profiles from Wang et al. (2016) can be modified to match our observations. However, the reason that photolysis was neglected by Wang et al. (2016) is that it is expected to primarily affect the upper troposphere ($p < 0.5$ bar), not the deeper regions probed in the $5\text{-}\mu\text{m}$ region (Strobel, 1977).

Alternatively, it is possible that the vertical mixing strength does not in fact decrease towards the poles. Wang et al. (2015) and Flasar and Gierasch (1978) focus on small-scale turbulent convection, and how this is affected by the increasing importance of rotation at high latitudes. While turbulent convection is inhibited towards the poles, it is possible that planetary-scale vertical motion increases. Solar heating is at a minimum at the poles, which reduces the static stability of the atmosphere and convection becomes uninhibited (Irwin, 2003). However, Wang et al. (2016) showed that PH_3 and AsH_3 are not sensitive to the strength of vertical mixing, while GeH_4 is. Even if the trend reported in Wang et al. (2015) and Flasar and Gierasch (1978) were to be reversed entirely, we would expect to see an increase of GeH_4 at the poles and a flat latitudinal distribution of AsH_3 and PH_3 , which is not what we observe.

It is also possible that the sensitivities of the disequilibrium species to K_{eddy} , as described in Wang et al. (2015), are not robust. In several cases, the authors note a lack of available kinetic data which limit the confidence in the results. However, these diffusion-kinetics calculations do provide a useful explanation for the difference in behaviour between GeH_4 and AsH_3/PH_3 . In addition, changes to the chemistry model cannot single-handedly account for the discrepancy between the theory and the observations. If AsH_3 and PH_3 were more sensitive to K_{eddy} , they would be predicted to decrease, not increase, towards the poles, since K_{eddy} decreases at high latitudes (Wang et al., 2015).

Finally, there is the possibility that our observational conclusions are incorrect. We have shown that there are several degeneracies which complicate the retrievals of gaseous abundances in Jupiter’s troposphere. Nevertheless, we are confident in the overall latitudinal trends that we report. The differences between the equatorial latitudes and the high latitudes are extremely apparent in the raw

observations themselves, even before we begin to model the spectra (Figures 12 and 15).

10. Conclusions

The CRIRES instrument on the VLT was used to make high-resolution ($R=96,000$) observations of Jupiter in the 5- μm window, where the planet's atmosphere is optically thin. This enabled us to spectrally resolve the line shapes of four minor species in Jupiter's troposphere: CH_3D , GeH_4 , AsH_3 and PH_3 . The slit was aligned north-south along Jupiter's central meridian, allowing us to search for latitudinal variability in these line shapes. The spectra were analysed using the NEMESIS radiative transfer code and retrieval algorithm. We make the following conclusions:

1. There are degeneracies between the cloud structure and scattering properties that complicate the retrievals of tropospheric gaseous abundances. These degeneracies can sometimes explain apparent belt-zone variations in composition. Any future studies into belt-zone variability must therefore carefully assess the degeneracies with the assumed scattering properties before any conclusions about spatial variations in gaseous abundances can be drawn.
2. As seen in Bjoraker et al. (2015), there is some evidence for the existence of a highly variable cloud deck at ~ 5 bar, but this conclusion is limited by degeneracies with cloud scattering properties.
3. We are able to fit all spatial regions with a GeH_4 abundance of 0.58 ppb, which is consistent with previous studies. We find that the AsH_3 abundance varies between 0.01 ppb and 0.55 ppb from equator to pole. This is the first time that supersolar abundances of AsH_3 have been measured in Jupiter's atmosphere. We measure a PH_3 abundance that varies between 0.5 and 1.5 ppm, which is consistent with previous measurements.
4. We found that GeH_4 appears to have an abundance that is constant with latitude, while PH_3 and AsH_3 show evidence for an enhancement at high latitudes. This partially agrees with a theoretical study from Wang et al. (2016) which suggests that GeH_4 should have a different latitudinal profile to PH_3 and AsH_3 . However, our observations disagree with the shapes of those profiles, as they predict that GeH_4 should decrease towards the poles while PH_3 and AsH_3 are flat. The explanation for this difference is not clear, but it could be due to the effect of photolytic destruction, increased global-scale convection at the poles, missing chemical kinetic data, or a combination thereof.

This study has demonstrated the utility of high-resolution 5- μm observations in studying Jupiter's mid-tropospheric composition, revealing the latitudinal distributions of arsine and germane for the first time. The

CRIRES observations were limited to central-meridian scans of the planet. Future work to explore Jupiter's deep atmosphere must utilise spatially-resolved spectral mapping to relate the dynamics of distinct atmospheric features to the distributions of these disequilibrium species.

Acknowledgements

Giles was supported via a Royal Society studentship, and Fletcher was supported via a Royal Society Research Fellowship at the University of Leicester. Irwin acknowledges the support of the United Kingdom Science and Technology Facilities Council. This work is based on observations collected at the European Organisation for Astronomical Research in the Southern Hemisphere under ESO programme 090.C-0053(A).

References

References

- Ballester, P., Banse, K., Castro, S., Hanuschik, R., Hook, R., Izzo, C., Jung, Y., Kaufer, A., Larsen, J., Licha, T., et al., 2006. Data reduction pipelines for the Very Large Telescope, in: Proc. SPIE.
- Berghund, M., Wieser, M.E., 2011. Isotopic compositions of the elements 2009 (IUPAC Technical Report). Pure and Applied Chemistry 83, 397–410.
- Bézard, B., Drossart, P., Lellouch, E., Tarrago, G., Maillard, J., 1989. Detection of arsine in Saturn. The Astrophysical Journal 346, 509–513.
- Bézard, B., Lellouch, E., Strobel, D., Maillard, J.P., Drossart, P., 2002. Carbon monoxide on Jupiter: evidence for both internal and external sources. Icarus 159, 95–111.
- Bjoraker, G., Wong, M., de Pater, I., Ádámkóvics, M., 2015. Jupiter's deep cloud structure revealed using keck observations of spectrally resolved line shapes. The Astrophysical Journal 810, 122.
- Bjoraker, G.L., Larson, H.P., Kunde, V.G., 1986. The gas composition of Jupiter derived from 5- μm airborne spectroscopic observations. Icarus 66, 579–609.
- Borysow, A., 1991. Modeling of collision-induced infrared absorption spectra of $\text{H}_2\text{-H}_2$ pairs in the fundamental band at temperatures from 20 to 300 K. Icarus 92, 273–279.
- Borysow, A., Frommhold, L., 1986. Theoretical collision-induced rototranslational absorption spectra for the outer planets: $\text{H}_2\text{-CH}_4$ pairs. The Astrophysical Journal 304, 849–865.
- Borysow, A., Frommhold, L., 1987. Collision-induced rototranslational absorption spectra of $\text{CH}_4\text{-CH}_4$ pairs at temperatures from 50 to 300 K. The Astrophysical Journal 318, 940–943.
- Borysow, J., Frommhold, L., Birnbaum, G., 1988. Collision-induced rototranslational absorption spectra of $\text{H}_2\text{-He}$ pairs at temperatures from 40 to 3000 K. The Astrophysical Journal 326, 509–515.
- Corice, R.J., Fox, K., 1972. The hypothetical chemical and spectroscopic activity of germane in the atmosphere of Jupiter. Icarus 16, 388–391.
- Cutri, R., Skrutskie, M., Van Dyk, S., Beichman, C., Carpenter, J., Chester, T., Cambresy, L., Evans, T., Fowler, J., Gizis, J., et al., 2003. 2MASS all sky catalog of point sources. .
- Dana, V., Mandin, J., Tarrago, G., Olson, W., Bézard, B., 1993. Absolute infrared intensities in the fundamentals ν_1 and ν_3 of arsine. Journal of molecular spectroscopy 159, 468–480.
- Drossart, P., Encrenaz, T., Kunde, V., Hanel, R., Combes, M., 1982. An estimate of the PH_3 , CH_3D , and GeH_4 abundances on Jupiter from the Voyager IRIS data at 4.5 μm . Icarus 49, 416–426.
- Drossart, P., Lellouch, E., Bézard, B., Maillard, J.P., Tarrago, G., 1990. Jupiter: Evidence for a phosphine enhancement at high northern latitudes. Icarus 83, 248–253.

- Encrenaz, T., de Graauw, T., Schaeidt, S., Lellouch, E., Feuchtgruber, H., Beintema, D., Bézard, B., Drossart, P., Griffin, M., Heras, A., et al., 1996. First results of ISO-SWS observations of Jupiter. *Astronomy and Astrophysics* 315, L397–L400.
- Fegley, B., Lodders, K., 1994. Chemical models of the deep atmospheres of Jupiter and Saturn. *Icarus* 110, 117–154.
- Ferris, J., Bossard, A., Khwaja, H., 1984. Mechanism of phosphine photolysis. application to jovian atmospheric photochemistry. *Journal of the American Chemical Society* 106, 318–324.
- Fink, U., Larson, H.P., Treffers, R.R., 1978. Germane in the atmosphere of Jupiter. *Icarus* 34, 344–354.
- Flasar, F.M., Gierasch, P.J., 1978. Turbulent convection within rapidly rotating superadiabatic fluids with horizontal temperature gradients. *Geophysical & Astrophysical Fluid Dynamics* 10, 175–212.
- Fletcher, L., Orton, G., Teanby, N., Irwin, P., 2009. Phosphine on Jupiter and Saturn from Cassini/CIRS. *Icarus* 202, 543–564.
- Giles, R.S., Fletcher, L.N., Irwin, P.G., 2015. Cloud structure and composition of Jupiter's troposphere from 5- μ m Cassini VIMS spectroscopy. *Icarus* 257, 457–470.
- Gillet, F., Low, F., Stein, W., 1969. The 2.8-14 micron spectrum of Jupiter. *The Astrophysical Journal* 157, 925.
- Grevesse, N., Asplund, M., Sauval, A., 2007. The solar chemical composition. *Space Science Reviews* 130, 105–114.
- Guillemin, J.C., Lassalle, L., Janati, T., 1995. Germane photochemistry. photolysis of gas mixtures of planetary interest. *Planetary and Space Science* 43, 75–81.
- Irwin, P., Parrish, P., Fouchet, T., Calcutt, S., Taylor, F., Simon-Miller, A., Nixon, C., 2004. Retrievals of jovian tropospheric phosphine from Cassini/CIRS. *Icarus* 172, 37–49.
- Irwin, P., Teanby, N., de Kok, R., Fletcher, L., Howett, C., Tsang, C., Wilson, C., Calcutt, S., Nixon, C., Parrish, P., 2008. The NEMESIS planetary atmosphere radiative transfer and retrieval tool. *Journal of Quantitative Spectroscopy and Radiative Transfer* 109, 1136–1150.
- Irwin, P., Weir, A., Smith, S., Taylor, F., Lambert, A., Calcutt, S., Cameron-Smith, P., Carlson, R., Baines, K., Orton, G., et al., 1998. Cloud structure and atmospheric composition of Jupiter retrieved from Galileo near-infrared mapping spectrometer real-time spectra. *Journal of Geophysical Research: Planets* (1991–2012) 103, 23001–23021.
- Irwin, P.G., 2003. *Giant Planets of Our Solar System*. Springer Praxis. chapter Mean and eddy circulation of the giant planet atmospheres.
- Jacquinet-Husson, N., Arie, E., Ballard, J., Barbe, A., Bjoraker, G., Bonnet, B., Brown, L., Camy-Peyret, C., Champion, J., Chedin, A., et al., 1999. The 1997 spectroscopic GEISA databank. *Journal of Quantitative Spectroscopy and Radiative Transfer* 62, 205–254.
- Jacquinet-Husson, N., Crepeau, L., Armante, R., Boutammine, C., Chédin, A., Scott, N., Crevoisier, C., Capelle, V., Boone, C., Poulet-Crovisier, N., et al., 2011. The 2009 edition of the GEISA spectroscopic database. *Journal of Quantitative Spectroscopy and Radiative Transfer* 112, 2395–2445.
- Käufl, H.U., Ballester, P., Biereichel, P., Delabre, B., Donaldson, R., Dorn, R., Fedrigo, E., Finger, G., Fischer, G., Franza, F., et al., 2004. CRIRES: a high resolution infrared spectrograph for ESO's VLT, in: *Proc. SPIE*.
- Kunde, V., Hanel, R., Maguire, W., Gautier, D., Baluteau, J., Marten, A., Chedin, A., Husson, N., Scott, N., 1982. The tropospheric gas composition of Jupiter's North Equatorial Belt (NH_3 , PH_3 , CH_3D , GeH_4 , H_2) and the jovian D/H isotopic ratio. *The Astrophysical Journal* 263, 443–467.
- Larson, H., Fink, U., Treffers, R., 1977. Phosphine in Jupiter's atmosphere - the evidence from high-altitude observations at 5 micrometers. *The Astrophysical Journal* 211, 972–979.
- Lellouch, E., Bézard, B., Fouchet, T., Feuchtgruber, H., Encrenaz, T., de Graauw, T., 2001. The deuterium abundance in Jupiter and Saturn from ISO-SWS observations. *Astronomy and Astrophysics* 370, 610–622.
- Lellouch, E., Drossart, P., Encrenaz, T., 1989. A new analysis of the jovian 5- μ m Voyager/IRIS spectra. *Icarus* 77, 457–465.
- Lepage, P., Champion, J.P., Robiette, A.G., 1981. Analysis of the ν_3 and ν_1 infrared bands of GeH_4 . *Journal of Molecular Spectroscopy* 89, 440–448.
- Lewis, J.S., Fegley, M.B., 1984. Vertical distribution of disequilibrium species in Jupiter's troposphere. *Space Science Reviews* 39, 163–192.
- Mandin, J., Dana, V., Tarrago, G., Klee, S., Winnewisser, B., 1995. Line positions and intensities in the vibrational system $2\nu_2/\nu_2+\nu_4/2\nu_4/\nu_1/\nu_3$ of arsine. *Journal of Molecular Spectroscopy* 172, 319–329.
- Noll, K.S., Geballe, T., Knacke, R., 1989. Arsine in Saturn and Jupiter. *The Astrophysical Journal* 338, L71–L74.
- Noll, K.S., Larson, H.P., Geballe, T., 1990. The abundance of AsH_3 in Jupiter. *Icarus* 83, 494–499.
- Plass, G.N., Kattawar, G.W., Catchings, F.E., 1973. Matrix operator theory of radiative transfer. 1: Rayleigh scattering. *Applied Optics* 12, 314–329.
- Ridgway, S., Wallace, L., Smith, G., 1976. The 800-1200 inverse centimeter absorption spectrum of Jupiter. *The Astrophysical Journal* 207, 1002–1006.
- Roos-Serote, M., Irwin, P., 2006. Scattering properties and location of the Jovian 5-micron absorber from Galileo/NIMS limb-darkening observations. *Journal of Quantitative Spectroscopy and Radiative Transfer* 101, 448–461.
- Rothman, L.S., Gordon, I.E., Barbe, A., Benner, D.C., Bernath, P.F., Birk, M., Boudon, V., Brown, L.R., Campargue, A., Champion, J.P., et al., 2009. The HITRAN 2008 molecular spectroscopic database. *Journal of Quantitative Spectroscopy and Radiative Transfer* 110, 533–572.
- Strobel, D., 1977. NH_3 and PH_3 photochemistry in the jovian atmosphere. *The Astrophysical Journal* 214, L97–L99.
- Taylor, F., Atreya, S., Encrenaz, T., Hunten, D., Irwin, P., Owen, T., 2004. *Jupiter: The Planet, Satellites and Magnetosphere*. Cambridge University Press. chapter The Composition of the Atmosphere of Jupiter. pp. 59–78.
- Wang, D., Gierasch, P.J., Lunine, J.I., Mousis, O., 2015. New insights on Jupiter's deep water abundance from disequilibrium species. *Icarus* 250, 154–164.
- Wang, D., Lunine, J.I., Mousis, O., 2016. Modeling the disequilibrium species for Jupiter and Saturn: Implications for Juno and Saturn entry probe. *Icarus* 276, 21–38.
- Wenger, C., Champion, J., 1998. Spherical top data system (STDS) software for the simulation of spherical top spectra. *Journal of Quantitative Spectroscopy and Radiative Transfer* 59, 471–480.
- Westphal, J., 1969. Observations of localised 5-micron radiation from Jupiter. *The Astrophysical Journal* 157, L63–L64.
- Wildt, R., 1932. *Absorptionsspektren und atmosphären der grossen planeten*. Veroeffentlichungen der Universitaets-Sternwarte zu Goettingen 2, 171.
- Wong, M.H., Mahaffy, P.R., Atreya, S.K., Niemann, H.B., Owen, T.C., 2004. Updated Galileo probe mass spectrometer measurements of carbon, oxygen, nitrogen, and sulfur on Jupiter. *Icarus* 171, 153–170.
- Zhang, X., West, R., Banfield, D., Yung, Y., 2013. Stratospheric aerosols on Jupiter from Cassini observations. *Icarus* 226, 159–171.